CRYSTAL GROWTH & DESIGN

pubs.acs.org/crystal

Article

Growth and Transformation of Hydrated Magnesium Carbonates under Near-Ambient Conditions

Ian Shortt, Vikram Gopalan, Jared Ura, Dylan Singh, Gaurav Sant, and Erika La Plante*

Cite This: *Cryst. Growth Des.* 2024, 24, 10193−10202

Read Online

ACCESS | Metrics & More | Article Recommendations | Supporting Information

ABSTRACT: Concrete composed of magnesium carbonates not only exhibits the potential for greater strength but also offers reduced carbon dioxide emissions compared with conventional concrete made with ordinary Portland cement. In a series of experiments conducted at various saturation ratios and near-ambient temperatures, hydrated magnesium carbonate phases were precipitated and subsequently analyzed by using a range of spectroscopic techniques. Hydrated magnesium carbonates, including nesquehonite ($MgCO_3 \cdot 3H_2O$) and hydromagnesite ($Mg_5(CO_3)_4(OH)_2 \cdot 4H_2O$), formed readily from the growth solutions. Time-resolved analysis using atomic force microscopy, Fourier-transform infrared spectroscopy, X-ray diffraction, and Raman spectroscopy revealed a correlation between the degree of solution supersaturation with respect to hydromagnesite and the delay in the transition from early-stage nesquehonite to hydromagnesite, suggesting that the increased concentration of magnesium cations impeded phase evolution. Furthermore, the introduction of the additives RbCl and CsCl accelerated this transformation. These observations can be explained by considering the influences of the ions in solution on the magnesium ion's dehydration energy. These findings are significant because they demonstrate a pathway for phase selection during magnesium carbonate precipitation at near-ambient temperatures. The results of this study have implications for carbon dioxide mineralization and the design of concrete that gains strength through the precipitation of magnesium carbonates.

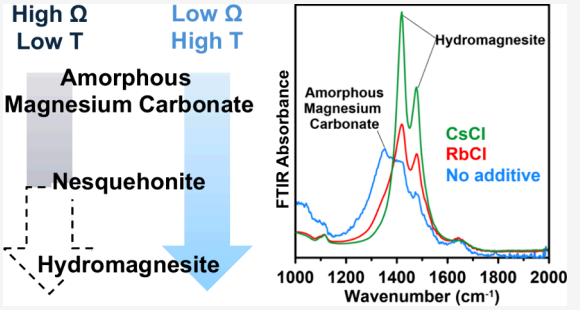

1. INTRODUCTION

Global emissions from the construction industry largely arise from cement production, generating approximately 0.9 t of carbon dioxide (CO_2) emissions per ton of cement produced.[1] Cement production alone contributes to about 8−9% of industrial global emissions.[2,3] This is mainly attributed to the production of the clinker during cement manufacturing. Calcination to form magnesia (MgO) requires far lower temperatures of around 600 °C.[3−5] The energy savings associated with this alternative process offer an opportunity to reduce emissions by lowering energy requirements during calcination and by capturing carbon using the produced magnesia.[6,7]

Magnesium carbonate cements offer several additional advantages, including comparable[8] or even greater[9] compressive strength than traditional Portland cement, compensation of thermal shrinkage,[10,11] and the ability to accelerate construction by continuously casting concrete without cold joints.[12] It is this array of qualities that has led to an increased interest, both academically and commercially, in magnesium carbonate cements. At present, the production of magnesium carbonate cement through the curing of MgO necessitates high humidity and elevated levels of carbon dioxide to yield cement that is suitable for construction purposes.[13] In the absence of these conditions, typically only brucite ($Mg(OH)_2$) precipitates,[8] resulting in strength that is unsuitable for construction. However, when magnesium carbonate cements are manufactured under optimal conditions, they cannot be cured on-site, restricting their use solely to precast applications that necessitate curing in a factory.[3]

Precipitation of magnesium carbonate phases has been extensively studied under supercritical conditions of temperature and pressure, which are the most relevant for long-term CO_2 storage[14,15] and which lead to accelerated precipitation of hydromagnesite for applications in construction materials.[16] However, the employment of supercritical conditions for carbonate precipitation requires significant energy and costs up to $50−$100 per ton.[17] Cementation arising from magnesium carbonate precipitation under near-ambient conditions is less studied, although rapid precipitation under these conditions enables industrial applications at low costs. Studies of precipitation of magnesium carbonate phases indicate that despite the simplicity of the stoichiometry, the kinetics is highly complex.[18,19] Although magnesite ($MgCO_3$) is the most

Received: July 31, 2024
Revised: November 25, 2024
Accepted: November 26, 2024
Published: December 9, 2024

Table 1. Description of the Experimental Conditions Employed in This Study, Showing the Concentration of Dissolved Magnesium, Carbon, Rubidium, and Cesium and Reaction Temperature Used as the Initial Conditions for Geochemical Modeling[a]

						saturation index							
[Mg] (mM)	[C] (mM)	[Rb] (mM)	[Cs] (mM)	T (°C)	pH	brucite	AMC	artinite	dypingite	hydromagnesite	lansfordite	nesquehonite	magnesite
20	20	0	0	75	7.55	−0.54		0.12	1.10	4.02		−1.09	2.43
50	50	0	0	50	7.51	−1.57		−0.52	0.01	3.15		−0.68	2.49
50	50	0	0	75	7.42	−0.54		0.58	2.93	5.85		−0.64	2.88
50	50	50	0	75	7.43	−0.55		0.54	2.83	5.74		−0.66	2.86
50	50	0	50	75	7.43	−0.55		0.54	2.83	5.75		−0.66	2.86
100	100	0	0	50	7.41	−1.58		−0.20	1.32	4.46		−0.35	2.82
100	100	0	0	75	7.32	−0.54		0.89	4.21	7.12		−0.32	3.20
200	200	0	0	25	7.47	−2.72	0.07	−1.08	−0.94	2.81	0.13	−0.31	2.73
200	200	0	0	50	7.30	−1.60		0.08	2.53	5.66		−0.05	3.13
200	200	0	0	75	7.22	−0.56		1.16	5.39	8.29		−0.03	3.51
500	500	0	0	75	7.06	−0.63		1.44	6.81	9.68		0.32	3.88

[a]The concentration of N is twice that of Mg, whereas the concentration of Na is equal to that of C. The calculated saturation indices with respect to brucite, amorphous magnesium carbonate (AMC), artinite, dypingite, hydromagnesite, lansfordite, nesquehonite, and magnesite are also shown. The reaction duration is 6 h for all experiments. The enthalpies of reaction (ΔH_R) are unknown for lansfordite and AMC, precluding the calculation of SI at $T \neq 25$ °C.

stable phase, under ambient conditions, its precipitation can take years,[20,21] leading researchers to explore other metastable phases such as nesquehonite ($MgCO_3{\cdot}3H_2O$) and hydromagnesite ($Mg_5(CO_3)_4(OH)_2{\cdot}4H_2O$)). Studies have shown that two primary pathways facilitate the transformation of magnesium carbonates: (i) dehydration of phases and (ii) dissolution−precipitation reactions, depending on the magnesium concentration in solution, wherein low concentrations favor dehydration and high concentrations favor dissolution−precipitation.[18,22]

Despite recent work on the precipitation of hydrated magnesium carbonate phases, several research questions remain, including how saturation indices and temperature affect phase selection and which pathways are operative during phase transformation. In this study, we performed experiments to induce magnesium carbonate precipitation under near-ambient conditions. Since previous work suggests that alkali metal salts favor magnesite formation and that this effect becomes more significant with increasing ionic size and decreasing hydration energy,[23,24] selected experimental conditions were also conducted in the presence of RbCl and CsCl. Analytical techniques, including atomic force microscopy (AFM), Fourier-transform infrared spectroscopy (FTIR), Raman spectroscopy, and X-ray diffraction (XRD), supplemented by geochemical modeling, were employed to study the phase evolution of hydrated magnesium carbonates and the effects of alkali metal-based additives on their precipitation. The observed relationships among the solution composition, reaction temperature, and the rate and extent of phase transformation, in the absence and presence of additives, provide insights into operative mechanisms during phase transformation. These results can be applied to optimize carbon dioxide mineralization through magnesium carbonate cementation.

2. MATERIALS AND METHODS

2.1. Sample Preparation. Samples were prepared by mixing stock solutions of magnesium nitrate hexahydrate ($Mg(NO_3)_2{\cdot}6H_2O$, 99% purity, 256.41 g/mol) and sodium bicarbonate ($NaHCO_3$, 99% purity, 84.007 g/mol), with ultrapure deionized (DI) water (ThermoFisher Scientific Barnstead Micropure, ≥18.20 MΩ·cm) used as the solvent. For the additive-containing samples, two stock solutions were prepared: (i) 100 mM $Mg(NO_3)_2{\cdot}6H_2O$ and 100 mM of the additive (either rubidium chloride (RbCl, 99% purity, 120.92 g/mol) or cesium chloride (CsCl, 99% purity, 168.36 g/mol)) and (ii) 100 mM $NaHCO_3$. Magnesium carbonate samples were prepared in two ways: either deposited on a mica substrate or as a bulk powder for use in XRD characterization. The experimental design employed dissolved Mg^{2+} and CO_3^{2-} ions rather than solid MgO and gaseous CO_2 to isolate the influences of MgO and CO_2 dissolution on the overall rates of magnesium carbonate precipitation, allowing focus on the kinetics of the precipitation process itself. For samples grown on mica, 1 mL of each stock solution was prepared in a 10 mL polypropylene tube for a total volume of 2 mL. A mica substrate (Ted Pella V1 grade, 10 mm in diameter) was immediately (within a few seconds) inserted into the resulting solution with final concentrations of Mg and total dissolved CO_2, [Mg] = [C], of either 50, 100, or 200 mM (Table 1), allowing for heterogeneous precipitation directly on the substrate. To ensure thermal equilibration, centrifuge tubes containing 1 mL of each stock solution were placed in a water bath for ∼15 min before mixing. The tubes containing the growth solutions were kept in the water bath to maintain a constant temperature of either 25, 50, or 75 °C for set periods of reaction time (i.e., 1, 30, 60, 120, and 360 min). The additive-containing growth solutions have a final solution composition of [Mg] = [C] = [Rb] or [Cs] = 50 mM and were left to react for 6 h at 75 °C. The growth solutions were not stirred during the reaction. Once the reaction interval was completed, the mica substrate was removed from the solution, and the excess moisture was removed by a brief exposure to ultrahigh-purity nitrogen gas. Once dried, the mica substrates were placed in sealed high-density polyethylene containers and stored under ambient conditions. One sample was prepared for each experimental condition.

The bulk powder samples were prepared by mixing stock solutions containing 1 M $Mg(NO_3)_2{\cdot}6H_2O$ and 1 M $NaHCO_3$, resulting in a growth solution with [Mg] = [C] = 500 mM. The growth solution was left to react for 6 h at 75 °C. The precipitates were allowed to settle at the bottom of the container and then separated from the residual solution by decanting. The samples were then dried in a vacuum oven at 25 °C for 1 week to completely remove water. The precipitates were then homogenized by manual grinding using an agate mortar and pestle before characterization.

Solution speciation and saturation indices of relevant phases were calculated using the geochemical modeling software, PHREEQC[25] with the *llnl* database, which contains thermodynamic data for brucite, various hydrated magnesium carbonate phases (artinite ($Mg_2CO_3(OH)_2{\cdot}3H_2O$), lansfordite, hydromagnesite, magnesite,

https://doi.org/10.1021/acs.cgd.4c01071
Cryst. Growth Des. 2024, 24, 10193−10202

nesquehonite), and the alkali metals used in this study. In addition, the solubility product (log K_{sp} = −34.93 at 25 °C, for $Mg_5(CO_3)_4(OH)_2{\cdot}H_2O$ = $5Mg^{2+}$ + $4CO_3^{2-}$ + $2OH^-$ + H_2O) and enthalpy of reaction (ΔH_R = −191.71 kJ/mol, estimated from the solubility products at 25 and 35 °C) for dypingite were added in the database using data from Harrison et al.,[26] whereas the solubility product at 25 °C for amorphous magnesium carbonate (log K_{sp} = −5.1804 at 25 °C, for $MgCO_3{\cdot}0.47H_2O$ = Mg^{2+} + CO_3^{2-} + $0.47H_2O$) was taken from Chang et al.[27] The initial solutions in the simulations considered the elemental concentrations of Mg, N, Na, and C, allowing for the calculation of pH through charge balance. The tendency for the precipitation of a given phase is given by the saturation index (SI) of the solution with respect to the phase and is defined as log Ω, where the saturation ratio, $\Omega = Q/K_{sp}$, where Q is the ion activity product and K_{sp} is the solubility product.

2.2. Characterization of Precipitates. Bulk powder specimens were analyzed by using a Bruker D8 Advance X-ray diffractometer with a Cu $K\alpha$ (1.54 Å) over scattering angles, 2θ, of 5−80°. The precipitates were frontloaded onto a silicon substrate for XRD measurements. The following parameters were employed: a step size of 0.02° in 2θ, count time per step of 0.3 s, current of 40 mA, and voltage of 40 kV. The substrate-grown samples were characterized by using a Nicolet is50 Fourier-transform infrared spectrometer (FTIR). Infrared spectra were collected for 32 background and sample scans with the atmospheric suppression option enabled over a range of 525−4000 cm^{-1}. These samples were also characterized using a Renishaw RM1000 confocal Raman microscope using the following parameters: 200−1200 cm^{-1} wavenumber range, 785 nm laser, 50× magnification, and 25% power. Ambient topographical imaging was conducted using a Cypher ES environmental atomic force microscope (Oxford Instruments Asylum Research) and a gold-plated probe with nominal characteristics: 225 μm length, 28 μm width, and resonance frequency of 75 kHz. Images were collected in the AC/tapping mode.

3. RESULTS AND DISCUSSION

3.1. Geochemical Modeling. A description of the experimental conditions and the modeled saturation indices of the as-mixed growth solutions is shown in Table 1. In general, the solutions are undersaturated in brucite and supersaturated in hydromagnesite and magnesite. The solution is slightly undersaturated with respect to nesquehonite, although supersaturation is observed when using a different thermodynamic database. The similarity between all of the experimental conditions is further supported by the observation of nesquehonite in all cases, even in growth solutions that show an undersaturation. These experimental conditions allow for the investigation of the precipitation kinetics of hydrated magnesium carbonate precipitation without the competition of brucite. Notably, although a solution having higher [Mg] and [C] was used to generate enough material for XRD characterization (Section 3.2), general trends in saturation indices remain the same.

In general, the reaction solution will evolve toward decreasing supersaturation with respect to magnesium carbonates, decreasing the rate of precipitation as time progresses. Our observations show that in the magnesium carbonate system, the degree of supersaturation is insufficient in predicting the specific phases that would form. For instance, increasing the concentrations of Mg and C increased both saturation indices with respect to hydromagnesite and nesquehonite but only promoted the persistence of nesquehonite (Section 3.2).

3.2. Growth and Transformation of Hydrated Magnesium Carbonates. The stepwise phase evolution in hydrated magnesium carbonates generally results in the following pathway: lansfordite ($MgCO_3{\cdot}5H_2O$), then nesquehonite ($MgCO_3{\cdot}3H_2O$), dypingite ($Mg_5(CO_3)_4(OH)_2{\cdot}5H_2O$), hydromagnesite ($Mg_5(CO_3)_4(OH)_2{\cdot}4H_2O$), and finally magnesite ($MgCO_3$).[13] Other magnesium carbonate phases also include artinite ($Mg_2(CO_3)(OH)_2{\cdot}3H_2O$), barringtonite ($MgCO_3{\cdot}2H_2O$), and amorphous magnesium carbonate (AMC). The extent to which these metastable hydrated magnesium carbonates are observed is a sensitive function of the specific environmental conditions,[28] and previous works show that a combination of thermodynamic and kinetic effects determines the progression of phase transformation.[29] For example, artinite and lansfordite are unlikely to form under our experimental conditions.[18,30−32] To assess which progression is observed under our experimental conditions, the XRD patterns of the samples grown from a solution containing [Mg] = [C] = 500 mM at 75 °C are compared with the reference XRD pattern of hydromagnesite and nesquehonite,[33,34] the most prevalent metastable phases of hydrated magnesium carbonate (Figure 1). X-ray diffractograms for dypingite and magnesite

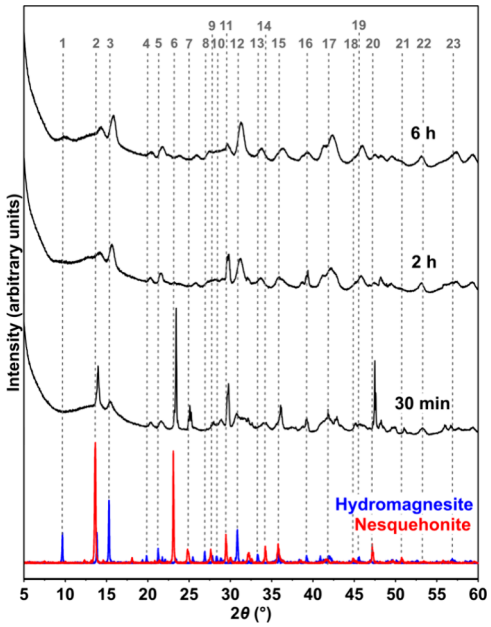

Figure 1. X-ray diffraction pattern of bulk powder samples formed from a growth solution containing [Mg] = [C] = 500 mM at 75 °C showing the transition from nesquehonite toward hydromagnesite. The reference spectra for hydromagnesite and nesquehonite are shown.[33,34] At 30 min, numerous characteristic nesquehonite peaks appear and then subsequently disappear or recede as reaction time increases. Conversely, numerous characteristic hydromagnesite peaks emerge over time.

do not match the observed patterns. The transformation from dominantly nesquehonite (at 30 min) to dominantly hydromagnesite (at 2 and 6 h) is evident from the notable decreases in the intensities of the peaks at 14, 23, 30, 35, and 47° (see Peaks 2, 6, 11, 14, and 20, respectively, in Figure 1), which are characteristic of nesquehonite.[33] Conversely, as the experiment progressed, characteristic hydromagnesite peaks such as at 15, 21, 26, and 31° (see Peaks 3, 5, 8, and 12, respectively, in Figure 1) became more prominent. The peak at 15° (see Peak 3) exemplifies this trend, displaying as a low-intensity peak at 30 min before increasing in intensity over time (Figure 1). It is also observed that numerous diffraction peaks are broad, indicating poor crystallinity and the presence of amorphous

https://doi.org/10.1021/acs.cgd.4c01071
Cryst. Growth Des. 2024, 24, 10193−10202

Table 2. Characteristic Wavenumbers of FTIR Absorbance Peaks of Magnesium Carbonates

peak labels	wavenumber (cm^{-1})	bond	associated phases	references
	800	CO_3^{2-} (bending)	hydromagnesite, dypingite	40
	850	CO_3^{2-} (bending)	hydromagnesite, dypingite	40,41
	880	CO_3^{2-} (bending)	hydromagnesite, dypingite	40,41
1	1350	CO_3^{2-} (symmetric stretching)	magnesium carbonates	37
2	1400−1420	CO_3^{2-} (asymmetric stretching)	magnesium carbonates	38,41
3	1470	CO_3^{2-} (asymmetric stretching)	hydrated magnesium carbonates	38,41,42
4	1515	CO_3^{2-} (asymmetric stretching)	nesquehonite	38,41,43
5	1641	O−H (in-plane bending)	water	43,44
6	2900−3600	O−H	water	40,42
7	3620	O−H	hydrated magnesium carbonates, brucite, muscovite	40,42,45

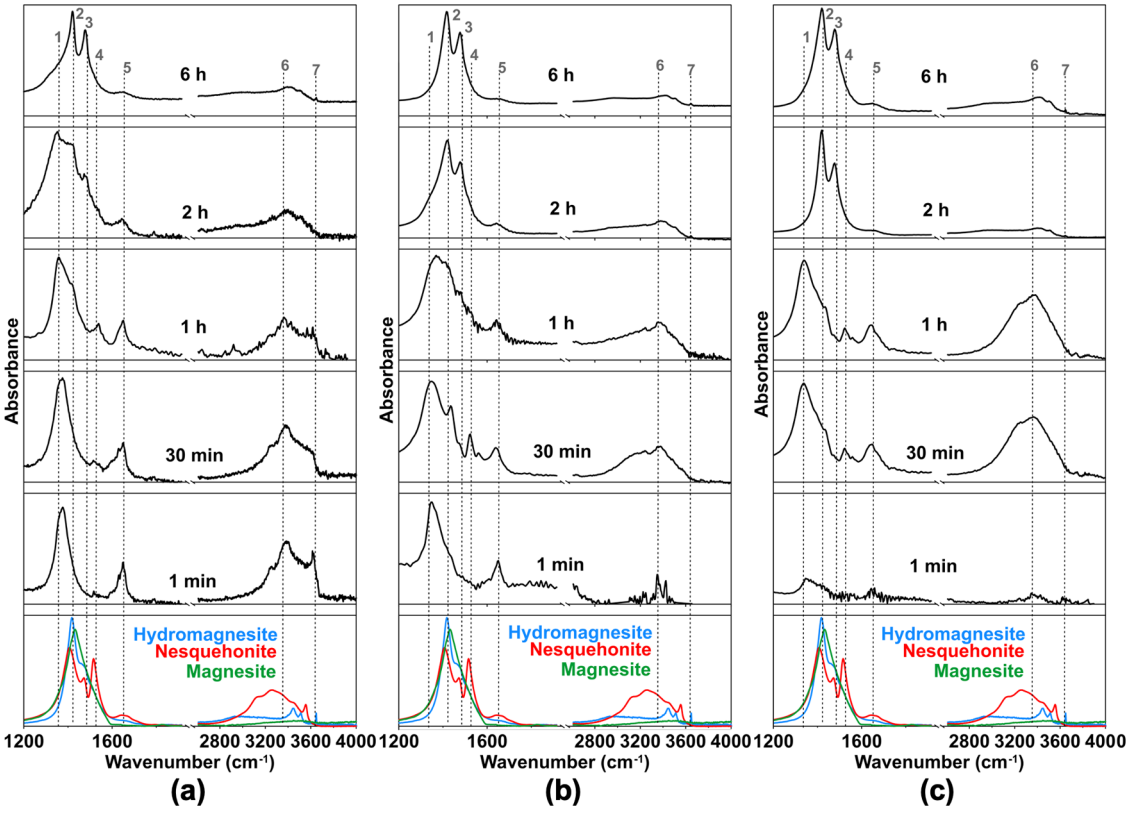

Figure 2. Representative FTIR spectra of magnesium carbonates grown on mica substrates from growth solutions containing (a) [Mg] = [C] = 50 mM, (b) [Mg] = [Rb] = [C] = 50 mM, and (c) [Mg] = [Cs] = [C] = 50 mM, reacted at 75 °C from 1 min to 6 h. Wavenumbers of primary importance are marked with dashed lines (Table 2).

phases. Amorphous magnesium carbonate has been observed to precipitate under similar conditions at lower temperatures ([Mg] = [C], 15 °C) for 416 h.[35] This suggests the successive formation of AMC, nesquehonite, and finally, hydromagnesite.

Among the primary FTIR peaks associated with magnesium carbonates (Table 2), of particular interest are the peaks present at 1350, 1400−1420, and 1515 cm^{-1}, whose appearance and disappearance provide insights into the phases present. Specifically, the carbonate peak at 1350 cm^{-1}[36] that forms early on may be associated with lansfordite[37] whereas the peak at 1515 cm^{-1} is characteristic of nesquehonite.[33,38] On the other hand, the peaks at 1400−1420 and 1470 cm^{-1} are characteristic of multiple hydrated magnesium carbonate phases such as hydromagnesite, nesquehonite, and dypingite, with the former peak present in all magnesium carbonates.[33,34,38,39] The absence of all other peaks between 1000 and 4000 cm^{-1} besides 1400−1420 cm^{-1} would therefore suggest the presence of magnesite.[39] The broad peak centered at 2900−3600 cm^{-1} suggests the presence of water within hydroxylated phases, whereas that at 3620 cm^{-1} is associated with brucite, which is not observed in our samples.

The FTIR spectra focused on the regions between ∼1200 to 2000 and ∼2800 to 4000 cm^{-1} because of overlap with peaks corresponding to the mica substrate at wavenumbers <1200 cm^{-1} (Figure 2). During the early stages of precipitation at 75 °C, specifically between 1 min to 1 h, peaks at 1350, 1515, and 1640 cm^{-1} are present (see Peaks 1, 4, and 5, respectively, in Figure 2a). Peaks 4 and 5 suggest the presence of nesquehonite, whereas Peak 1 suggests that another early-stage hydrated magnesium carbonate phase may be briefly appearing. Although the peak position reasonably matches that of lansfordite,[38] this phase does not typically precipitate at temperatures greater than 10 °C.[46] Furthermore, the presence of poorly crystalline phases as evident from XRD and the

https://doi.org/10.1021/acs.cgd.4c01071
Cryst. Growth Des. 2024, 24, 10193−10202

presence of irregularly shaped nanoparticles visible in the AFM micrographs at short reaction times suggest that Peak 1 represents amorphous magnesium carbonate that initially forms before transforming briefly to nesquehonite then hydromagnesite, a known precipitation pathway for magnesium carbonates.[35] The characteristic nesquehonite peak at 1515 cm^{-1} decreased in relative intensity over time, suggesting a corresponding decrease in the amount of the phase. After 2 h of reaction, Peaks 1 (1420 cm^{-1}) and 2 (1470 cm^{-1}) are most prominent, whereas Peaks 1 and 4 begin to recede until they largely vanish after 6 h, indicating the transformation from nesquehonite to hydromagnesite (Figure 2a), consistent with the XRD results (Figure 1). This agrees with the Ostwald Rule of Stages and known phase transformation behavior associated with hydrated magnesium carbonates.[13] Peaks 5 (1640 cm^{-1}), 6 (2900−3600 cm^{-1}), and 7 (3620 cm^{-1}) are indicative of the hydrated nature of the precipitated carbonate.

At lower reaction temperatures, i.e., $T \leq 50$ °C, nesquehonite persists even after 6 h of reaction, as evidenced by the presence of the peaks at 1350 and 1515 cm^{-1} (e.g., see Peaks 1 and 4, respectively, in the precipitates grown from solutions containing [Mg] = [C] = 200 mM at 50 °C) (Figure 3). Similarly, higher concentrations (i.e., greater degrees of supersaturation) also slowed down the phase transition (e.g., compare spectra for [Mg] = [C] = 50 mM vs 200 mM at 50 °C in Figure 3). These trends persist at different reaction times (not shown). This can be partially explained by magnesium's resistance to dehydration due to the multiple solvation shells around the cation. At near-ambient temperatures, water exchange mechanisms in magnesium's hydration shell occur through either direct or indirect exchange.[47] This exchange is limited by the strength of magnesium's hydration shells,[20,48] consistent with its high hydration energy,[49] as well as the inability of the water molecules trapped in the hydration shells to form hydrogen acceptor bonds.[41] Subsequently, the dehydration that is necessary for the phase transition could be impeded by the increasing concentration of magnesium cations in solution, as water exchange becomes more limited. Additionally, the decrease in transformation rate toward hydromagnesite with increasing magnesium concentration suggests that dissolution−precipitation may be the dominant mechanism[22] and that the rate-limiting step (either dissolution or precipitation) may change as the concentration increases.[50] Moreover, higher temperatures (and vibrational energies) promote phase evolution by increasing the rate at which water exchange occurs in the hydration shell of magnesium.[47] A similar temperature dependence in hydrated magnesium carbonate phase evolution has been observed previously.[15,18]

The Raman spectra of hydromagnesite, nesquehonite, and magnesite are similar, with primary differences in peak positions within 200−1200 cm^{-1}. In hydromagnesite, the CO_3^{2-} symmetric stretching mode shifts from a lower wavenumber (Peak 9, 1094 cm^{-1}) to a higher wavenumber (Peak 10, 1121 cm^{-1}), whereas this peak is shifted to the lower value in nesquehonite[33,43] and magnesite[39,51] (Table 3). Within this range of wavenumbers, magnesite is very similar to nesquehonite,[33] but the former can be identified through the absence of O−H peaks at higher wavenumbers between 1600 and 1700 and 3200−3600 cm^{-1} (Table 3).

By comparing with peaks associated with magnesium carbonates (Table 3), Raman spectra show the evolution of the phase from what appears to be a precursor magnesium carbonate with nesquehonite characteristics toward hydro-

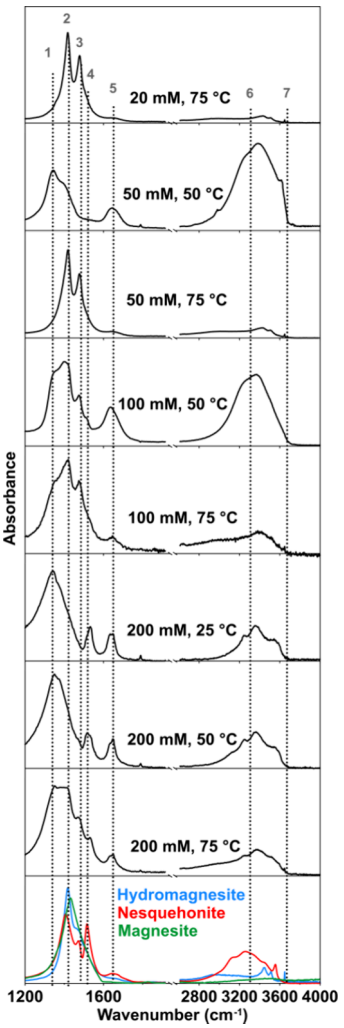

Figure 3. Representative FTIR spectra of magnesium carbonates precipitated on mica substrates from growth solutions containing [Mg] = [C] ranging from 20 to 200 mM and temperatures ranging from 50 to 75 °C for 6 h (Table 1). The wavenumbers of primary importance are labeled by dashed lines (Table 2).

Table 3. Characteristic Wavenumbers of Raman Peaks of Magnesium Carbonates

peak labels	wavenumber (cm^{-1})	bond	associated phases	references
1	261	O−Al−O, O−Si−O	muscovite	52,53
2	407	O−Al−O, O−Si−O	muscovite	52,53
3	635	HCO_3^- (in-plane bending)	nesquehonite	33,54
4	705	CO_3^{2-} (in-plane bending)	magnesium carbonates	54,55
5	758	CO_3^{2-} (in-plane bending)	magnesium carbonates	54,55
6	910	CO_3^{2-} (out-of-plane bending)	nesquehonite	33
7	952	CO_3^{2-} (out-of-plane bending)	nesquehonite	33
8	1055	CO_3^{2-} (symmetric stretching)	nesquehonite	33,56
9	1094	CO_3^{2-} (symmetric stretching)	nesquehonite, magnesite	33,37,39,57
10	1121	CO_3^{2-} (symmetric stretching)	hydromagnesite	54

https://doi.org/10.1021/acs.cgd.4c01071
Cryst. Growth Des. 2024, 24, 10193−10202

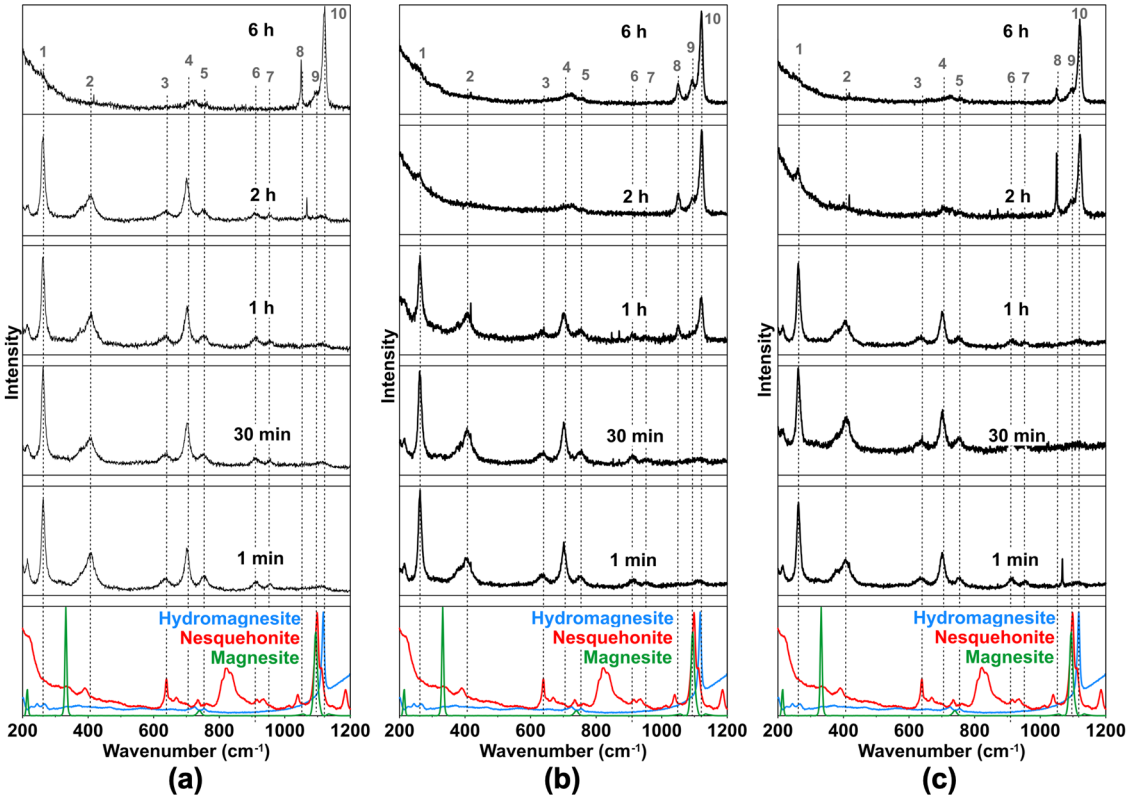

Figure 4. Representative Raman spectra of magnesium carbonates grown on mica substrates from growth solutions containing (a) [Mg] = [C] = 50 mM, (b) [Mg] = [Rb] = [C] = 50 mM, and (c) [Mg] = [Cs] = [C] = 50 mM, reacted at 75 °C from 1 min to 6 h. Wavenumbers of primary importance are marked by dashed lines (Table 3).

magnesite (compare 1 min vs 6 h of reaction time in Figure 4a). Characteristic peaks for nesquehonite are located at 642, 910, 955, and 1094 cm^{-1} and persist for up to 2 h of reaction (Peaks 3, 6, 7, and 9, respectively, in Figure 4a). After 6 h of reaction, the spectra match those of hydrated magnesium carbonates, where the primary peaks of interest that remain are those at 705, 758, and 1121 cm^{-1} (Peaks 4, 5, and 10, respectively, in Figure 4a). Each of these peaks is associated with carbonates, either in-plane bending for Peaks 4 and 5 or symmetric stretching for Peak 10. The Raman peaks located at 261 and 407 cm^{-1} (Peaks 1 and 2, rspectively) are characteristic of the muscovite mica substrate.[52,53] The early presence and then subsequent disappearance of these peaks are due to the magnesium carbonate precipitates eventually fully covering up the mica substrate.

Our observations generally agree with previous literature. At temperatures above 60 °C, hydromagnesite is prevalent, at both high and low concentrations.[18,58] Increasing temperature was observed to increase the rate of transformation toward hydromagnesite as well as the degree of precipitation.[18,20,59,60] Conversely, at temperatures of 50 °C and below, the decrease in temperature results in a delay in transformation toward hydromagnesite. The experiments at 25 °C resulted in the formation of nesquehonite despite the predicted supersaturation of hydromagnesite, consistent with a previous work wherein nesquehonite was observed to precipitate under similar conditions.[18] Hydromagnesite was observed to form under some of these conditions but in lesser quantities and always with amorphous magnesium carbonates and nesquehonite present as intermediate phases.[20]

3.3. Influence of Rb and Cs on the Growth of Magnesium Carbonate.

Raman and FTIR spectroscopies were used to understand how the monovalent ions Rb^+ and Cs^+ affect the precipitation of hydrated magnesium carbonates. Compared with the additive-free samples, those that were formed in the presence of additives showed a faster transformation to hydromagnesite under otherwise equivalent experimental conditions (Figures 2 and 4). Note that the saturation indices are not significantly altered in the presence of additives (Table 1). FTIR spectra show that the peaks associated with hydromagnesite (e.g., Peaks 2 and 3 in Figure 2) emerge sooner than in the additive-free sample (Figure 2a), specifically at 30 min rather than between 1 and 2 h of reaction (Figure 2b,c). Furthermore, the Raman spectra of both additive-containing cases (Figure 4b,c) reveal the persistence of hydromagnesite within 2 h of reaction (e.g., compare Peaks 3 and 10 in Figure 4b,c with Figure 4a) instead of 6 h. Previous work suggests that it is possible to reduce the time required for the precipitation of magnesite by decreasing the activity and thickness of the magnesium hydration shell.[61,62] Other investigators have studied the effect of specific alkali metal cations such as K^+ and found that their addition greatly accelerated the phase transition toward magnesite from hydromagnesite by disrupting the hydration shells of the magnesium ion.[23] The acceleration of hydromagnesite formation in the presence of RbCl and CsCl can be explained by the decrease in the dielectric constant of the reaction solution,[63] which reduces the solvation energy or dehydration energy of magnesium as described by the Born equation.[64] This has been previously demonstrated for magnesium

https://doi.org/10.1021/acs.cgd.4c01071
Cryst. Growth Des. 2024, 24, 10193−10202

carbonate precipitated from aqueous solutions with ethanol replacement.[19]

Notably, a shoulder at 1350 cm^{-1} (Peak 1), indicative of an earlier magnesium carbonate phase such as AMC, is present in both the control sample and the Rb-containing sample after 2 h but not in the Cs-containing sample (Figure 2), suggesting a greater extent of hydromagnesite formation in the latter. The greater acceleration for CsCl suggests that the larger ionic size and lower hydration energy of Cs^+ compared to Rb^+[49] facilitated the disruption of the Mg^{2+} hydration shell more effectively.

3.4. Morphological Observations. The phase transformation indicated by XRD, FTIR, and Raman corresponds to morphological changes as observed using AFM (Figure 5). After 1 min, amorphous nanoparticles begin to form (Figure 5a) in addition to elongated precipitates characteristic of nesquehonite[65] but are more blade-like than needle-like (red arrows in Figure 5). The nesquehonite-like carbonate persisted in the 30 min sample, as evidenced by the same morphology (Figure 5b). In addition, small amounts of sheet-like precipitates also started to form (yellow arrows in Figure 5). Based on their morphology, these are either dypingite or hydromagnesite, which form into either loose platelets or a more tightly bound rosette structure constructed from platelets.[66] Based on the XRD (Figure 1), FTIR (Figures 2 and 3), and Raman spectroscopy (Figure 4) results, we posit these precipitates to be hydromagnesite. After 1 h, nesquehonite is observed precipitating alongside hydromagnesite (Figure 5c). This is evident from the characteristic platelet structures growing from the nesquehonite blades (see features marked by yellow arrows in Figure 5c). At 2 h, hydromagnesite precipitates begin to grow to a few microns in height, with only a few nesquehonite blades remaining (Figure 5d). Finally, after 6 h, the dominant phase is hydromagnesite, identified by the characteristic rosette structure of interlocking plates forming ridges (Figure 5e).[67] Observations from scanning electron microscopy of selected precipitates are consistent with the AFM observations (Supporting Information).

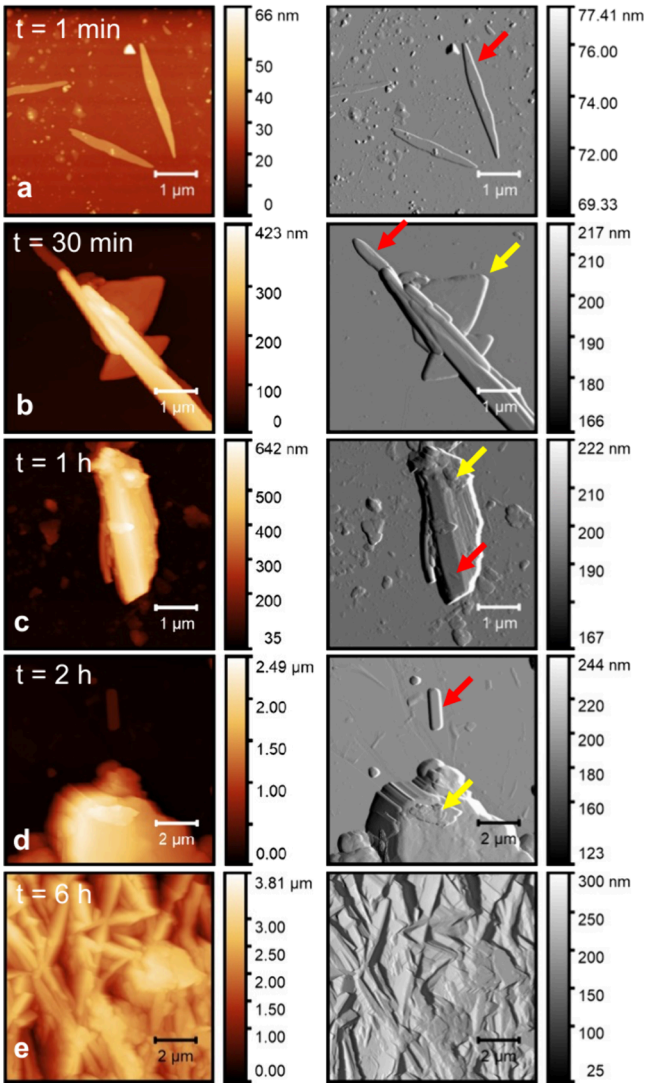

Figure 5. Representative AFM micrographs of magnesium carbonate precipitates deposited on a mica substrate reacted with a growth solution containing [Mg] = [C] = 50 mM at 75 °C for (a) 1 min, (b) 30 min, (c) 1 h, (d) 2 h, and (e) 6 h. Topography (height) images are displayed on the left, and amplitude error images are shown on the right. Red arrows mark blade-like features, suggestive of nesquehonite, whereas yellow arrows mark platelet-like features, suggestive of hydromagnesite.

The micrographs in Figure 5 suggest that the magnesium carbonate precipitates form by dissolution–precipitation. This is most directly visible in Figure 5c, where nesquehonite blades are observed alongside interlocking hydromagnesite platelets, suggesting interfacial dissolution–precipitation from nesquehonite to hydromagnesite.[68,69] It has been shown that, under similar environmental conditions, hydromagnesite can form both by direct precipitation from solution and through the transformation of nesquehonite.[41]

4. CONCLUSIONS

We systematically analyzed the phase evolution of hydrated magnesium carbonates under near-ambient conditions as well as the effect of alkali metal cation additives on the phase evolution. While this study is focused on short-term precipitation (i.e., on a time frame of hours) rather than long-term (i.e., on a time frame of days to years), the analysis presented herein provides key insights into how solution composition and temperature influence the rate and extent of phase transformation via influences on the hydration shells of magnesium ions. Specifically, FTIR, XRD, Raman spectroscopy, and AFM simultaneously confirm precipitation pathway models, where nesquehonite precipitates before it transitions into hydromagnesite. The transition from nesquehonite to hydromagnesite is delayed at high supersaturations, while hydromagnesite is dominant at low supersaturations, presumably due to water exchange limitations as a result of increased magnesium concentrations. Analogous experiments in the presence of alkali cations, RbCl and CsCl, resulted in accelerated phase transformation to hydromagnesite, potentially by decreasing the dielectric constant and solvation energy of Mg^{2+} as observed previously for ethanol–water mixtures. These learnings can be applied in designing chemical admixtures for carbonate cementation that achieve rapid room-temperature hydromagnesite precipitation.

■ ASSOCIATED CONTENT

Supporting Information

The Supporting Information is available free of charge at https://pubs.acs.org/doi/10.1021/acs.cgd.4c01071.

https://doi.org/10.1021/acs.cgd.4c01071
Cryst. Growth Des. 2024, 24, 10193−10202

Representative scanning electron microscopy images of magnesium carbonate precipitates and methodology employed (PDF)

AUTHOR INFORMATION

Corresponding Author

Erika La Plante − *Department of Materials Science and Engineering, University of California, Davis, Davis, California 95616, United States;* orcid.org/0000-0002-5273-9523; Email: eclaplante@ucdavis.edu

Authors

Ian Shortt − *Department of Materials Science and Engineering, University of Texas at Arlington, Arlington, Texas 76019, United States; Department of Materials Science and Engineering, University of California, Davis, Davis, California 95616, United States*

Vikram Gopalan − *Department of Materials Science and Engineering, University of California, Davis, Davis, California 95616, United States*

Jared Ura − *Department of Materials Science and Engineering, University of California, Davis, Davis, California 95616, United States*

Dylan Singh − *Department of Materials Science and Engineering, University of Texas at Arlington, Arlington, Texas 76019, United States*

Gaurav Sant − *Institute for Carbon Management, Department of Civil and Environmental Engineering, Department of Materials Science and Engineering, and California NanoSystems Institute, University of California, Los Angeles, Los Angeles, California 90095, United States;* orcid.org/0000-0002-1124-5498

Complete contact information is available at: https://pubs.acs.org/10.1021/acs.cgd.4c01071

Notes

The authors declare no competing financial interest.

ACKNOWLEDGMENTS

The authors gratefully acknowledge the financial support provided by the National Science Foundation through the CAREER Award #2342381 and the U.S. Department of Energy's Advanced Research Projects Agency-Energy (ARPA-E: AMENDER: DE-AR0001551 and RECLAIM: DE-AR0001777). This work was conducted at the Materials Chemistry Laboratory (MCL) and the Keck Spectral Imaging Facility at the University of California, Davis, and the Characterization Center for Materials and Biology (CCMB) at the University of Texas at Arlington. The authors express their appreciation for the support that has facilitated the operations of these laboratories. The contents of this paper represent the views and opinions of the authors, who are responsible for the accuracy of the datasets presented herein. They do not reflect the views and/or policies of the funding agency, nor do the contents constitute a specification, standard, or regulation.

REFERENCES

(1) Hottle, T.; Hawkins, T. R.; Chiquelin, C.; Lange, B.; Young, B.; Sun, P.; Elgowainy, A.; Wang, M. Environmental Life-Cycle Assessment of Concrete Produced in the United States. *J. Clean. Prod.* **2022**, *363*, No. 131834.

(2) Lamb, W. F.; Wiedmann, T.; Pongratz, J.; Andrew, R.; Crippa, M.; Olivier, J. G. J.; Wiedenhofer, D.; Mattioli, G.; Khourdajie, A. A.; House, J.; Pachauri, S.; Figueroa, M.; Saheb, Y.; Slade, R.; Hubacek, K.; Sun, L.; Ribeiro, S. K.; Khennas, S.; De La Rue Du Can, S.; Chapungu, L.; Davis, S. J.; Bashmakov, I.; Dai, H.; Dhakal, S.; Tan, X.; Geng, Y.; Gu, B.; Minx, J. A Review of Trends and Drivers of Greenhouse Gas Emissions by Sector from 1990 to 2018. *Environ. Res. Lett.* **2021**, *16* (7), No. 073005.

(3) Walling, S. A.; Provis, J. L. Magnesia-Based Cements: A Journey of 150 Years, and Cements for the Future? *Chem. Rev.* **2016**, *116* (7), 4170−4204.

(4) Shorcht, Frauke; Kourti, I.; Scalet, B. M.; Roudier, S.; Sancho, L. D. *Best Available Techniques (BAT) Reference Document for the Production of Cement, Lime and Magnesium Oxide: Industrial Emissions Directive 2010/75/EU (Integrated Pollution Prevention and Control)*; Publications Office: LU, 2013.

(5) Song, G.; Ding, Y.-D.; Zhu, X.; Liao, Q. Carbon Dioxide Adsorption Characteristics of Synthesized MgO with Various Porous Structures Achieved by Varying Calcination Temperature. *Colloids Surf. Physicochem. Eng. Asp.* **2015**, *470*, 39−45.

(6) Gartner, E.; Sui, T. Alternative Cement Clinkers. *Cem. Concr. Res.* **2018**, *114*, 27−39.

(7) Rakhimova, N. Calcium and/or Magnesium Carbonate and Carbonate-Bearing Rocks in the Development of Alkali-Activated Cements − A Review. *Constr. Build. Mater.* **2022**, *325*, No. 126742.

(8) Liska, M.; Al-Tabbaa, A. Ultra-Green Construction: Reactive Magnesia Masonry Products. *Proc. Inst. Civ. Eng. - Waste Resour. Manag.* **2009**, *162* (4), 185−196.

(9) Zhang, H.; Cao, M.; Chen, K.; Shen, C.; Xi, P.; Zhang, F.; Wang, S. Study on Material Properties of Magnesium Oxide Carbonized Prestressed Pipe Piles. *Adv. Civ. Eng.* **2018**, *2018*, 1−7.

(10) Zhang, J. Recent Advance of MgO Expansive Agent in Cement and Concrete. *J. Build. Eng.* **2022**, *45*, No. 103633.

(11) Li, Z.; Qian, J.; Qin, J.; Hua, Y.; Yue, Y.; Tang, H. Cementitious and Hardening Properties of Magnesia (MgO) under Ambient Curing Conditions. *Cem. Concr. Res.* **2023**, *170*, No. 107184.

(12) Du, C. A Review of Magnesium Oxide in Concrete. *Concr. Int.* **2005**, *27*, 45.

(13) Rheinheimer, V.; Unluer, C.; Liu, J.; Ruan, S.; Pan, J.; Monteiro, P. XPS Study on the Stability and Transformation of Hydrate and Carbonate Phases within MgO Systems. *Materials* **2017**, *10* (1), 75.

(14) Giammar, D. E.; Bruant, R. G.; Peters, C. A. Forsterite Dissolution and Magnesite Precipitation at Conditions Relevant for Deep Saline Aquifer Storage and Sequestration of Carbon Dioxide. *Chem. Geol.* **2005**, *217* (3−4), 257−276.

(15) Prigiobbe, V.; Mazzotti, M. Precipitation of Mg-Carbonates at Elevated Temperature and Partial Pressure of CO2. *Chem. Eng. J.* **2013**, *223*, 755−763.

(16) Kuenzel, C.; Zhang, F.; Ferrándiz-Mas, V.; Cheeseman, C. R.; Gartner, E. M. The Mechanism of Hydration of MgO-Hydromagnesite Blends. *Cem. Concr. Res.* **2018**, *103*, 123−129.

(17) Sanna, A.; Uibu, M.; Caramanna, G.; Kuusik, R.; Maroto-Valer, M. M. A Review of Mineral Carbonation Technologies to Sequester CO_2. *Chem. Soc. Rev.* **2014**, *43* (23), 8049−8080.

(18) Hänchen, M.; Prigiobbe, V.; Baciocchi, R.; Mazzotti, M. Precipitation in the Mg-Carbonate System—Effects of Temperature and CO2 Pressure. *Chem. Eng. Sci.* **2008**, *63* (4), 1012−1028.

(19) Fang, Y.; Zhang, F.; Farfan, G. A.; Xu, H. Low-Temperature Synthesis of Disordered Dolomite and High-Magnesium Calcite in Ethanol−Water Solutions: The Solvation Effect and Implications. *ACS Omega* **2022**, *7* (1), 281−292.

(20) Santos, H. S.; Nguyen, H.; Venâncio, F.; Ramteke, D.; Zevenhoven, R.; Kinnunen, P. Mechanisms of Mg Carbonates Precipitation and Implications for CO_2 Capture and Utilization/Storage. *Inorg. Chem. Front.* **2023**, *10* (9), 2507−2546.

(21) Hobbs, F. W. C.; Xu, H. Magnesite Formation through Temperature and pH Cycling as a Proxy for Lagoon and Playa Paleoenvironments. *Geochim. Cosmochim. Acta* **2020**, *269*, 101−116.

(22) Zhang, P.; Anderson, H. L.; Kelly, J. W.; Krumhansl, J. L.; Papenguth, H. W. *Kinetics and Mechanisms of Formation of Magnesite from Hydromagnesite in Brine*; 2000. https://www.osti.gov/servlets/purl/764025.
(23) Dong, W.; Liu, R.; Zhao, H.; Han, X. Preparation and Characterization of Anhydrous Magnesium Carbonate under the Present of Potassium Ions Solution. *Powder Technol.* **2020**, *360*, 741−746.
(24) Sandengen, K.; Jøsang, L. O.; Kaasa, B. Simple Method for Synthesis of Magnesite (MgCO3). *Ind. Eng. Chem. Res.* **2008**, *47* (4), 1002−1004.
(25) Parkhurst, D. L.; Appelo, C. A. J. Description of Input and Examples for PHREEQC Version 3—a Computer Program for Speciation, Batch-Reaction, One-Dimensional Transport, and Inverse Geochemical Calculations. In *Modeling techniques*; U.S. Geological Survey: **2013**, *6*, 497.
(26) Harrison, A. L.; Mavromatis, V.; Oelkers, E. H.; Bénézeth, P. Solubility of the Hydrated Mg-Carbonates Nesquehonite and Dypingite from 5 to 35 °C: Implications for CO2 Storage and the Relative Stability of Mg-Carbonates. *Chem. Geol.* **2019**, *504*, 123−135.
(27) Chang, C.-Y.; Yang, S.-Y.; Chan, J. C. C. Solubility Product of Amorphous Magnesium Carbonate. *J. Chin. Chem. Soc.* **2021**, *68* (3), 476−481.
(28) Kristova, P.; Hopkinson, L. J.; Rutt, K. J.; Hunter, H. M. A.; Cressey, G. Carbonate Mineral Paragenesis and Reaction Kinetics in the System MgO−CaO−CO2−H2O in Presence of Chloride or Nitrate Ions at near Surface Ambient Temperatures. *Appl. Geochem.* **2014**, *50*, 16−24.
(29) Chaka, A. M.; Felmy, A. R.; Qafoku, O. *Ab Initio* Thermodynamics of Magnesium Carbonates and Hydrates in Water-Saturated Supercritical CO2 and CO2-Rich Regions. *Chem. Geol.* **2016**, *434*, 1−11.
(30) Dell, R. M.; Weller, S. W. The Thermal Decomposition of Nesquehonite MgCO3· 3H2O and Magnesium Ammonium Carbonate MgCO3·(NH4)2CO3· 4H2O. *Trans. Faraday Soc.* **1959**, *55* (0), 2203−2220.
(31) Rincke, C.; Schmidt, H.; Voigt, W. A New Hydrate of Magnesium Carbonate, MgCO3·6H2O. *Acta Crystallogr., Sect. C: Struct. Chem.* **2020**, *76* (Pt3), 244.
(32) Ming, D. W.; Franklin, W. T. Synthesis and Characterization of Lansfordite and Nesquehonite. *Soil Sci. Soc. Am. J.* **1985**, *49* (5), 1303−1308.
(33) RRUFF Project *Nesquehonite R050639*, n.d. https://rruff.info/Nesquehonite/R050639.
(34) RRUFF Project *Hydromagnesite R060011*, n.d. https://rruff.info/Hydromagnesite/R060011.
(35) Tanaka, J.; Kawano, J.; Nagai, T.; Teng, H. Transformation Process of Amorphous Magnesium Carbonate in Aqueous Solution. *J. Mineral. Petrol. Sci.* **2019**, *114* (2), 105−109.
(36) Li, S.; Shi, Y.; Zeng, H.; Cai, N. Development of Carboxyl-Layered Double Hydrotalcites of Enhanced CO2 Capture Capacity by K2CO3 Promotion. *Adsorption* **2017**, *23* (2−3), 239−248.
(37) Coleyshaw, E. E.; Crump, G.; Griffith, W. P. Vibrational Spectra of the Hydrated Carbonate Minerals Ikaite, Monohydrocalcite, Lansfordite and Nesquehonite. *Spectrochim. Acta. A. Mol. Biomol. Spectrosc.* **2003**, *59* (10), 2231−2239.
(38) Jones, G. C.; Jackson, B. *Infrared Transmission Spectra of Carbonate Minerals*; Springer Netherlands: Dordrecht, 1993. .
(39) RRUFF Project *Magnesite R040114*, n.d. https://rruff.info/magnesite/display=default/R040114.
(40) Raade, G. Dypingite, a New Hydrous Basic Carbonate of Magnesium, from Norway. *J. Earth and Planet. Mater.* **1970**, *55*, 1457−1465.
(41) Hopkinson, L.; Rutt, K.; Cressey, G. The Transformation of Nesquehonite to Hydromagnesite in the System CaO-MgO-H_2O-CO_2: An Experimental Spectroscopic Study. *J. Geol.* **2008**, *116* (4), 387−400.
(42) Choi, S.-B.; Kim, N.-W.; Lee, D.-K.; Yu, H. Growth Mechanism of Cubic MgO Granule via Common Ion Effect. *J. Nanosci. Nanotechnol.* **2013**, *13* (11), 7577−7580.
(43) Frost, R. L.; Palmer, S. J. Infrared and Infrared Emission Spectroscopy of Nesquehonite Mg(OH)(HCO3)·2H2O−Implications for the Formula of Nesquehonite. *Spectrochim. Acta. A. Mol. Biomol. Spectrosc.* **2011**, *78* (4), 1255−1260.
(44) Shahabi-Navid, M.; Cao, Y.; Svensson, J. E.; Allanore, A.; Birbilis, N.; Johansson, L. G.; Esmaily, M. On the Early Stages of Localised Atmospheric Corrosion of Magnesium−Aluminium Alloys. *Sci. Rep.* **2020**, *10* (1), 20972.
(45) RRUFF Project *Brucite R040077*; https://rruff.info/brucite/R040077.
(46) Langmuir, D. STABILITY OF CARBONATES IN THE SYSTEM MgO-CO2-H20. *J. Geol.* **1965**, *73* (5), 730−754.
(47) Schwierz, N. Kinetic Pathways of Water Exchange in the First Hydration Shell of Magnesium. *J. Chem. Phys.* **2020**, *152* (22), 224106.
(48) Xu, J.; Yan, C.; Zhang, F.; Konishi, H.; Xu, H.; Teng, H. H. Testing the Cation-Hydration Effect on the Crystallization of Ca−Mg−CO_3 Systems. *Proc. Natl. Acad. Sci. U. S. A.* **2013**, *110* (44), 17750−17755.
(49) Rodriguez-Cruz, S. E.; Jockusch, R. A.; Williams, E. R. Hydration Energies and Structures of Alkaline Earth Metal Ions, M2+(H2O)n, n = 5−7, M = Mg, Ca, Sr, and Ba. *J. Am. Chem. Soc.* **1999**, *121* (38), 8898−8906.
(50) Pokharel, R.; Popa, I. C.; De Kok, Y.; King, H. E. Enhanced Nesquehonite Formation and Stability in the Presence of Dissolved Silica. *Environ. Sci. Technol.* **2024**, *58* (1), 362−370.
(51) Montes-Hernandez, G.; Renard, F. Time-Resolved in Situ Raman Spectroscopy of the Nucleation and Growth of Siderite, Magnesite, and Calcite and Their Precursors. *Cryst. Growth Des.* **2016**, *16* (12), 7218−7230.
(52) Singha, M.; Singh, L. Vibrational Spectroscopic Study of Muscovite and Biotite Layered Phyllosilicates. *Indian J. Pure Appl. Phys.* **2016**, *54*, 116−122.
(53) RRUFF Project *Muscovite R040104*, n.d. https://rruff.info/muscovite/R040104.
(54) Frost, R. L. Raman Spectroscopic Study of the Magnesium Carbonate Mineral Hydromagnesite ($Mg_5[(CO_3)_4(OH)_2]\cdot 4H_2O$). *J. Raman Spectrosc.* **2011**, *42* (8), 1690−1694.
(55) Frost, R. L.; Bahfenne, S.; Graham, J. Raman Spectroscopic Study of the Magnesium-Carbonate Minerals − Artinite and Dypingite. *J. Raman Spectrosc.* **2009**, *40*, 855.
(56) Frost, R. L. A Raman Spectroscopic Study of Selected Minerals of the Rosasite Group. *J. Raman Spectrosc.* **2006**, *37* (9), 910−921.
(57) Skliros, V.; Tsakiridis, P.; Perraki, M. A Combined Raman, Fourier Transform Infrared, and X-ray Diffraction Study of Thermally Treated Nesquehonite. *J. Raman Spectrosc.* **2020**, *51* (9), 1445−1453.
(58) Botha, A.; Strydom, C. A. Preparation of a Magnesium Hydroxy Carbonate from Magnesium Hydroxide. *Hydrometallurgy* **2001**, *62* (3), 175−183.
(59) Case, D. H.; Wang, F.; Giammar, D. E. Precipitation of Magnesium Carbonates as a Function of Temperature, Solution Composition, and Presence of a Silicate Mineral Substrate. *Environ. Eng. Sci.* **2011**, *28* (12), 881−889.
(60) Deng, C.; Liu, W.; Chu, G.; Luo, D.; Zhang, G.; Wang, L.; Yue, H.; Liang, B.; Li, C. Aqueous Carbonation of MgSO4 with (NH4)2CO3 for CO2 Sequestration. *Greenh. Gases Sci. Technol.* **2019**, *9* (2), 209−225.
(61) Power, I. M.; Kenward, P. A.; Dipple, G. M.; Raudsepp, M. Room Temperature Magnesite Precipitation. *Cryst. Growth Des.* **2017**, *17* (11), 5652−5659.
(62) Christ, C. L.; Hostetler, P. B. Studies in the System MgO-SiO2-CO2-H2O (II): The Activity-Product Constant of Magnesite. *Am. J. Sci.* **1970**, *268* (5), 439−453.
(63) Wei, Y.; Chiang, P.; Sridhar, S. Ion Size Effects on the Dynamic and Static Dielectric Properties of Aqueous Alkali Solutions. *J. Chem. Phys.* **1992**, *96* (6), 4569−4573.

https://doi.org/10.1021/acs.cgd.4c01071
Cryst. Growth Des. 2024, 24, 10193−10202

(64) Atkins, P. W.; MacDermott, A. J. The Born Equation and Ionic Solvation. *J. Chem. Educ.* **1982**, *59* (5), 359.
(65) Davies, P. J.; Bubela, B. The Transformation of Nesquehonite into Hydromagnesite. *Chem. Geol.* **1973**, *12* (4), 289−300.
(66) Wang, Y.; Liu, J.; Shi, T.; Yang, B.; Li, C.; Xu, H.; Yin, W. Preparation, Properties and Phase Transition of Mesoporous Hydromagnesite with Various Morphologies from Natural Magnesite. *Powder Technol.* **2020**, *364*, 822−830.
(67) Li, Q.; Ding, Y.; Yu, G.; Li, C.; Li, F.; Qian, Y. Fabrication of Light-Emitting Porous Hydromagnesite with Rosette-like Architecture. *Solid State Commun.* **2003**, *125* (2), 117−120.
(68) Rausis, K.; Ćwik, A.; Casanova, I. Phase Evolution during Accelerated CO2 mineralization of Brucite under Concentrated CO2 and Simulated Flue Gas Conditions. *J. CO2 Util.* **2020**, *37*, 122−133.
(69) Hopkinson, L.; Kristova, P.; Rutt, K.; Cressey, G. Phase Transitions in the System MgO−CO2−H2O during CO2 Degassing of Mg-Bearing Solutions. *Geochim. Cosmochim. Acta* **2012**, *76*, 1−13.

https://doi.org/10.1021/acs.cgd.4c01071
Cryst. Growth Des. 2024, 24, 10193−10202